# Supplementary Information for

**Measurements of the self-assembly kinetics of individual viral capsids around their RNA genome**

**Rees F. Garmann, Aaron M. Goldfain, and Vinothan N. Manoharan**

**Vinothan N. Manoharan**
**E-mail: vnm@seas.harvard.edu**

**This PDF file includes:**

Supplementary text
Figs. S1 to S17
Captions for Movies S1 to S5
References for SI reference citations

**Other supplementary materials for this manuscript include the following:**

Movies S1 to S5

**Supporting Information Text**

**Materials**

**Buffer recipes.**

**Assembly buffer** 42 mM Tris-HCl, pH 7.5; 84 mM NaCl; 3 mM acetic acid; 1 mM EDTA

**Hybridization buffer** 50 mM Tris-HCl, pH 7.0; 200 mM NaCl; 1 mM EDTA

**TAE buffer** 40 mM Tris-acetic acid, pH 8.3; 1 mM EDTA

**TNE buffer** 50 mM Tris-HCl, pH 7.5; 100 mM NaCl; 1 mM EDTA

**TE buffer** 10 mM Tris-HCl, pH 7.5; 1 mM EDTA

**Methods**

**Assessing the concentration and purity of MS2 virus particles, and of isolated coat protein and RNA.** We grow wild-type MS2 (a gift from Peter Stockley at the University of Leeds) by infecting liquid cultures of *E. coli* strain C3000 (also a gift from Peter Stockley) and purifying the progeny viruses following the protocols of Strauss and Sinsheimer [1]. We determine the concentration of MS2 by UV-spectrophotometry (NanoDrop-1000, Thermo Scientific), assuming an extinction coefficient of 8.03 mL mg$^{-1}$ cm$^{-1}$ at 260 nm (Ref. [1]). We store the purified virus particles (MW 3.6 MDa) in TNE buffer (50 mM Tris-HCl, pH 7.5; 100 mM NaCl; 1 mM EDTA) at 4 °C and discard them after about 1 month.

We purify coat-protein dimers ($2 \times 13.7 = 27.4$ kDa) from the virus particles following the cold acetic acid method described by Sugiyama, Hebert, and Hartmann [2]. Then we exchange the coat-protein buffer for 20 mM acetic acid using 3-kDa-MWCO centrifugal filter units (EMD Millipore). In 20 mM acetic acid, the coat proteins form non-covalent dimers [3]. We determine the concentration of coat-protein dimers by UV-spectrophotometry, using an extinction coefficient of 33200 M$^{-1}$ cm$^{-1}$ at 280 nm (Ref. [3]). We check for RNA contamination by measuring the ratio of the UV-absorbance at 260 nm to that at 280 nm (Fig. S12). We use only protein that has a 260/280 ratio less than 0.67 for assembly. We store the protein in 20 mM acetic acid at 4 °C, and discard it after 1 week.

We purify MS2 RNA (1.1 MDa) from freshly grown virus particles using an RNA extraction kit (RNeasy, Qiagen). We collect the RNA in TE buffer and determine its concentration by UV-spectrophotometry using an extinction coefficient of 0.025 mL mg$^{-1}$ cm$^{-1}$ at 260 nm. We check for protein contamination by measuring the ratio of the UV-absorbance at 260 nm to that at 280 nm (Fig. S12). We use only RNA that has a 260/280 ratio greater than 2.0 for assembly. Then we check the integrity of the RNA by native 1% agarose gel electrophoresis (Fig. S11). We store the RNA in TE buffer (10 mM Tris-HCl, pH 7.5; 1 mM EDTA) at $-80$ °C, and discard it after about 1 year.

**Interferometric scattering microscope.** Our microscope is is similar to the setup described by Ortega-Arroyo and coworkers [4]. A 450 nm, 100 mW, single-mode diode laser (PD-01251, Lasertack) illuminates the sample. The current driving the laser is modulated with a square wave at a frequency of 1 MHz to decrease the coherence of the laser and limit intensity variations in the background [5]. The beam (shown in blue in Fig. S13) is spatially filtered by a polarization-maintaining single-mode optical fiber (fiber 1; PM-S405-XP, Thorlabs). The filtered light is collected by a lens (lens 1; achromatic doublet, focal length 25 mm, Thorlabs), reflected from a polarizing beamsplitter cube (CCM1-PBS251, Thorlabs), and focused onto the back aperture of the objective (100× oil-immersion, 1.45 NA Plan Apo $\lambda$, Nikon) to produce collimated illumination in the imaging chamber. The light that is backscattered from the sample and light that is reflected from the water-coverslip interface are collected by the objective and imaged onto camera 1 (MV1-D1024E-160-CL, Photon Focus) by the tube lens (achromatic doublet, focal length 300 mm, Thorlabs). We use achromatic half and quarter-wave plates (AHWP3 and AQWP3, Bolder Vision Optik) with the polarizing beamsplitter to make an optical isolator that minimizes the intensity lost at the beamsplitter. The total magnification is 150×, such that each pixel on the camera views a field of 70 nm. All images are recorded with a bit depth of 12.

The illumination intensity, set to approximately 3 kW/cm$^2$ when we record data at 1,000 Hz and 0.3 kW/cm$^2$ at 100 Hz, is similar to that typically used in single-molecule fluorescence experiments [6]. To minimize any possible radiation damage, we use an exposure time that is almost equal to the total time between frames, and we dim the imaging beam with absorptive filters so that the camera pixels are nearly saturated. The total field of view is 140 pixels × 140 pixels (9.8 μm × 9.8 μm) at 1,000 Hz and 200 pixels × 200 pixels (14 μm × 14 μm) at 100 Hz.

We use short-wavelength light ($\lambda = 450$ nm) because the intensity of the image scales with $\lambda^{-2}$. While shorter wavelength lasers are available, we find that they can damage both the sample and optical components when used at high intensities. Control experiments at different illumination intensities are described in the Supplementary Text and Fig. S14.

In our microscope, the imaging beam is slightly misaligned to reduce back-reflections from the objective and the roof of the imaging chamber. To keep the point-spread function of the microscope symmetric, we set the misalignment as small as possible such that back-reflections from the objective do not overlap with the reference beam on the camera. To accomplish this, we first align the imaging beam with the microscope axis, and then we offset fiber 1 laterally using a two-axis linear translation stage (Thorlabs) and tilt the imaging beam using a mirror mounted in a two-axis kinematic mount (Thorlabs) located between lens 1 and the half-wave plate.

**Rees F. Garmann, Aaron M. Goldfain, and Vinothan N. Manoharan**

To minimize vibrations and long-term mechanical drift, we make the imaging beam path as short as possible, we mount the apparatus on an isolated optical table (RS4000, Newport), and we secure all cables going to non-isolated equipment using clamps that we line with semi-rigid foam (0.75-in-thick polyethylene; 8865K522, McMaster-Carr). To minimize thermal drift and the effects of air currents, we cover the entire apparatus in a foam-core box. We also allow all electronics associated with the microscope to warm up for a few hours before starting an experiment, so that any thermal gradients can equilibrate.

The coverslip and flow cells are mounted on a motorized three-axis stage (MAX343, Thorlabs) that has stepper motors for coarse adjustments and piezoelectric actuators for fine adjustments. The fine adjustments are used for active stabilization.

**Active stabilization.** The position of the coverslip relative to the objective is actively stabilized to a few nanometers in all three dimensions. Each dimension is controlled separately through a proportional control loop on the PC. During each iteration of the loop, the position of the coverslip is measured, and the voltage driving the piezoelectric actuators is modified to keep the coverslip in its original position.

The height of the coverslip above the objective is measured by tracking the position of a laser (red in Fig. S13) that is totally internally reflected by the coverslip-water interface, as described by Ortega-Arroyo and coworkers (4). We use a 785-nm, 90 mW, single-mode diode laser (L785P090, Thorlabs) that is coupled through a single-mode fiber (fiber 2; S630-HP, Thorlabs). The laser is driven with a constant current (27 mA) that is well below threshold (35 mA), which we find improves the intensity stability of the laser. After exiting the optical fiber, the beam is collected by lens 2 (plano-convex, focal length 20 mm, Thorlabs), reflects from a dichroic mirror (700-nm short-pass, Edmund Optics), and is focused onto the back aperture of the objective. We align the beam so that after exiting the objective, it totally internally reflects from the coverslip-water interface and re-enters the objective. The total power incident on the coverslip is less than 1 μW. The return beam reflects from the coverslip and then from a D-shaped mirror (Thorlabs) and is detected with camera 2 (DCC1545M, Thorlabs). A long-pass filter (700 nm, Thorlabs) attenuates any light from the imaging beam that is also incident on camera 2. When the height of the coverslip changes, the return beam is displaced laterally across camera 2, resulting in a change in the measured center-of-brightness. Under active stabilization, any changes in the center-of-brightness are measured and corrected every 30 ms.

The in-plane position of the coverslip is measured by tracking a 30-nm gold particle that is adsorbed to the coverslip surface (see Coverslip Functionalization below for details of how we prepare the coverslips). Before each experiment, we find one of the adsorbed gold particles by looking for spots that have a normalized intensity of approximately 0.2. We then move the coverslip so that the spot is near the edge of the field of view. Using a 16 × 16-pixel region of the field of view, we record a static background image of the coverslip with no particles present and then move the gold particle into the center of this small field of view. Before tracking the position of the gold particle, we process its image in the small field of view by subtracting off the static background, applying a bandpass filter (passing features of size 1 to 7 pixels) to smooth the image, and taking the time-median of 33 images of the particle (recorded at 33 Hz) to reduce shot noise. We then use the program Trackpy (7) to locate the position of the particle. We use this position for the active stabilization loop, which runs once per second. The in-plane control loop frequency (1 Hz) is lower than that of the out-of-plane control loop (33 Hz) because of the time required to collect the median image of the particle.

The active stabilization loops are implemented in a Python script (http://github.com/manoharan-lab/camera-controller). The same script includes a real-time image processing routine that allows us to see growing MS2 particles while collecting data.

**Intensity calibration.** We measure the intensities of MS2 RNA and wild-type MS2 virus particles (Fig. S2) by imaging the particles as they adsorb to an APTES-functionalized coverslip. For these experiments we use a "lean-to" sample chamber (8) made of 1-mm-thick glass slides (Micro Slides, Corning) that are cut, cleaned by pyrolysis (PYRO-CLEAN, Tempyrox Co.), and sealed in place with vacuum grease (High vacuum grease, Dow Corning). To perform the calibration experiment, we first fill the sample chamber with TNE buffer and focus the microscope onto the coverslip. We then exchange the buffer in the sample chamber with a solution containing both MS2 RNA and wild-type MS2 virus particles at a concentration of 0.1 nM each in TNE buffer. We record movies (100 Hz) of these particles nonspecifically adsorbing to the coverslip.

We see two well-separated populations in the distribution of intensities of the particles that bind (Fig. S2). We assume that the lower-intensity population is due to the RNA strands and the higher-intensity population is due to the virus particles, and we define the two intensity distributions using an intensity threshold (0.003) that lies between them. As stated in the main text, we infer the intensity distribution corresponding to the wild-type capsids by convolving the intensity distribution of the wild-type particles with the negative of the intensity distribution of the RNA. We use this inferred intensity distribution to estimate the intensity of full capsids that assemble in our experiments.

**Coverslip functionalization.** We adapt the protocols described by Joo and Ha (9) to coat glass coverslips with a layer of PEG molecules, about 1% of which are functionalized with short DNA oligonucleotides. We find that many brands of #2 coverslips are unsuitable for assembly measurements because they have imperfections that scatter too much light. We use only #2 thickness, 24 mm × 60 mm rectangular glass microscope coverslips from Globe Scientific, Inc.

To functionalize the coverslips, we first treat them with (3-aminopropyl)triethoxysilane (APTES, 99%, Sigma-Aldrich) to impart a positive surface charge when the coverslips are submerged in neutral-pH buffer. The coverslips can then nonspecifically bind oppositely charged macroions such as nucleic acids and MS2 capsids, as shown in Fig. S2. Furthermore, the layer of amino groups can form covalent linkages through *N*-hydroxysuccinimide (NHS) chemistry. We form the PEG layer by adding 90 μL of 100 mM sodium bicarbonate buffer containing 9 mg of a 100:1 mixture of 5,000-Da NHS-PEG (>95%, Nanocs)

and 5,000-Da NHS-PEG-N$_3$ (purity unreported, Nanocs) between two APTES-functionalized coverslips and then letting the "sandwich" sit overnight at room temperature in a humid box before washing the slips with deionized water (obtained from a Millipore RNase-free system; Synthesis, Milli-Q). We attach DNA oligonucleotides to the surface-bound NHS-PEG-N$_3$ molecules by copper-free click chemistry. The 20-base-long oligonucleotides are synthesized with a dibenzocyclooctyne (DBCO) group on the 5$'$-end (RNase-free HPLC purified, Integrated DNA Technologies). We place 90 μL of 10 μM DBCO-DNA in phosphate-buffered saline (PBS without Ca or Mg, Lonza) between two coverslips and let the sandwich sit overnight at room temperature in a humid box. The sequence of the surface oligonucleotide is 5$'$-(DBCO)-GGTTGGTTGGTTGGTTGGTT-3$'$.

We test that the coverslips are functionalized with the surface oligonucleotide by measuring the specific binding of MS2 RNA that is hybridized to a complementary linker oligonucleotide using interferometric scattering microscopy, as described in the RNA-coverslip binding subsection below and Fig. S16.

Following functionalization, we decorate the coverslips with 30-nm gold particles that serve as tracer particles for active stabilization. We purchase 30-nm amine-functionalized particles (Nanopartz) and conjugate them to NHS-PEG to prevent adsorption of coat proteins. The conjugation is done by adding 20 mg of NHS-PEG to 200 μL of 10 nM of gold particles in 100 mM sodium bicarbonate buffer. The mixture is left overnight in a tube rotator. The particles are then washed five times by centrifuging the mixture at 8,000 g for 5 min and then resuspending in TE buffer. To allow the the PEG-passivated gold particles to bind nonspecifically to the coverslip, we sandwich 70 μL of 0.1 nM suspension of the particles between two coverslips and let them sit for 10 min at room temperature before washing the slips with deionized water. The method produces an average surface density of about 1 particle per 100 μm$^2$, as measured in the interferometric scattering microscope. Functionalized coverslips are stored under nitrogen gas at $-20$ °C and discarded after 2 months.

**Surface-immobilization of MS2 RNA by DNA linkages.** To immobilize MS2 RNA at the coverslip surface, we first hybridize the 5$'$-end of the RNA to a 60-base-long linker oligonucleotide (Integrated DNA Technologies). The 40 bases at the 5$'$-end of the linker are complementary to the 40 bases at the 5$'$-end of the RNA, and the remaining 20 bases are complementary to the sequence of the surface oligonucleotide (Fig. S15). To anneal the linker to the MS2 RNA, we add about 5 μM of the linker oligonucleotide to 100 nM MS2 RNA in hybridization buffer, heat the mixture to 90 °C for 1 s, and then cool it to 4 °C at a rate of $-1$ °C/s. We then dilute the mixture to 500-μL in hybridization buffer. Excess linker is removed with a 500-μL 100-kDa-MWCO centrifugal filter unit (EMD Millipore) at 14,000 g. We repeat the dilution and filtration steps three more times. We find that the 60-base-long oligonucleotides do not pass through the filter; instead, they stick to the membrane. We confirm RNA-DNA binding by native 1% agarose gel electrophoresis (Fig. S11). We confirm that the RNA-DNA constructs specifically bind our DNA-functionalized coverslips by interferometric scattering microscopy (Fig. S16). The sequence of the linker is 5$'$-CGACAGGAAGTTGAGCAGGACCCCGAAAGGGGTCCCACCCAACCAACCAACCAACCAACC-3$'$.

**Flow cell design and construction.** We build chips that each contain 10 separate flow cells above a single coverslip. Each chip consists of two sheets of cut, clear acrylic that are sealed together and to the coverslip with melted Parafilm (Bemis). Each flow cell has an imaging chamber that is used for the assembly experiments, an inlet cup to hold fluid before it is introduced into the imaging chamber of the flow cell, a short inlet chamber to connect the inlet cup to the imaging chamber, and an outlet chamber (Fig. S17). We use acrylic, a hard plastic, because we find that soft materials such as polydimethylsiloxane lead to more warping of the coverslip during injection of the protein.

A schematic of each of the layers of the chip, a cross sectional view of a single flow cell, and a photograph of the final assembled state are shown in Fig. S17. The bottom acrylic sheet (Optix Acrylic, ePlastics) is 0.75 mm thick and contains 10 rectangular through-holes (1 mm × 4.6 mm) that are cut with a laser cutter (HSE 150W, KERN). These rectangular holes form the imaging chamber of each flow cell. The top acrylic sheet (6.35 mm thick cast acrylic, McMaster-Carr) serves as the roof of the imaging chambers and contains the inlet cups, the inlet chambers, and the outlet chambers. Each inlet cup is 3.35 mm deep and 4 mm in diameter. Each inlet chamber is a 1-mm-diameter through-hole that begins at the base of an inlet cup and connects to an imaging chamber in the bottom acrylic sheet. The outlet chambers are 1.6-mm-diameter through-holes. We epoxy (5 minute epoxy, Devcon) a 10-mm-long aluminum tube (inner diameter 0.9 mm, outer diameter 1.6 mm, McMaster-Carr) into each outlet chamber. All holes in the top acrylic piece are machined with a mill. The Parafilm sheets used to seal together the layers of the flow cell contain rectangular gaps that are the same size as the imaging chambers. The gaps are cut with a computer-controlled vinyl cutter (CAMM-1 Servo, Roland).

To assemble each chip, we first clean the acrylic sheets and Parafilm by sonicating in a 2% w/v aqueous solution of sodium dodecyl sulfate (>99%, Sigma-Aldrich) for 30 min. After sonicating, we rinse the acrylic and Parafilm with deionized water and then dry them under a stream of nitrogen gas. Next, we press one sheet of Parafilm onto the bottom acrylic sheet so that the Parafilm and acrylic stick together, and we place this assembly in a 65 °C oven for 5 min. The top acrylic sheet is also placed in the oven for 5 min. When we remove the acrylic sheets from the oven and press them firmly together, the melted Parafilm seals the two sheets of acrylic together to form the chip. We then press the other sheet of Parafilm onto the bottom of the chip so that it sticks, and we place the chip in a 65 °C oven for 5 min. We remove the chip from the oven and press it firmly onto the functionalized coverslip (which is not heated) to seal the chip to the coverslip. We use all of the flow cells on a coverslip within one or two days.

We inject buffer solution into each imaging chamber using a plastic syringe (3 mL BD, VWR) that is connected to the aluminum outlet tube by a short (approximately 4 cm) length of tubing (Tygon PVC, McMaster-Carr). We fill the inlet cup with solution and then pull it through the imaging chamber by actuating the syringe with a motorized linear translation stage (PT1-Z8, Thorlabs). Each time we inject a solution into the imaging chamber, we use the motorized stage to inject 10 μL of

**Rees F. Garmann, Aaron M. Goldfain, and Vinothan N. Manoharan**

solution at a constant rate over 20 s. Before further injections we use a Kimwipe (Kimberly-Clark Professional) to wick any remaining solution from the inlet cup. To ensure that the fluid injection is reproducible, we prevent any air bubbles from entering the flow cell, tubing, or syringe. We mount the syringe vertically to prevent air bubbles from being trapped inside it.

**Assembly experiments.** For assembly experiments, we fill a flow cell with hybridization buffer containing 0.2% Tween-20 (Sigma-Aldrich) and let it sit for 10 min. We find that this 10-min incubation with Tween-20 prevents the MS2 coat protein from adsorbing to the coverslip through defects in the PEG layer. Next, we flush out the Tween-20 with fresh hybridization buffer, find the center of the imaging chamber, focus the microscope onto the coverslip, and begin the out-of-plane active stabilization control loop. Then we locate a 30-nm gold particle within 50 μm of the center of the imaging chamber and start the in-plane active stabilization control loop. With the setup actively stabilized in all three dimensions, we inject 1 nM RNA-DNA complexes in hybridization buffer and record a short movie of them adsorbing to the coverslip. After 10–100 complexes bind, we flush the imaging chamber by pumping 120 μL of assembly buffer through the chamber over the course of 12 min. Then we start recording a movie and inject the coat-protein dimers in assembly buffer. The injection starts 4 s into the movie.

The protein concentration we use is influenced by our choice of buffer conditions. We choose our assembly buffer (pH 7.5 and 125 mM monovalent ions) to reflect the expected pH and ionic composition *in vivo*, not because we claim that the assembly pathways we see are the same as those *in vivo*, but because these are the conditions under which we expect the interactions to be optimal for assembly. Given these buffer conditions, we use protein concentrations that are large enough (greater than 1 μM of dimers) for assembly to occur within the timescale of the experiment, but not so large (less than 4 μM dimers) that overgrown structures dominate.

Carey and Uhlenbeck (10) showed that varying the pH and ionic composition affects the strength of MS2 protein-RNA binding, and thus the protein concentration threshold for assembly. Previous work by Peter Stockley's group (3) used an assembly buffer with the same pH as our buffer but with much fewer ions (50 mM monovalent ions). As a result, the protein-RNA interactions in their experiments should be stronger than in ours, and the protein concentration threshold for assembly should be lower. Indeed, their experiments show assembly at 100–200 nM dimers, roughly an order of magnitude lower than in ours. These results highlight the importance of buffer conditions in determining the kinetics of assembly.

**Image processing.** We process the images to normalize them and to reduce fluctuations in the background intensity. We apply an approach similar to the "pseudo-flat-fielding" method described by Ortega-Arroyo and coworkers (4). The images in Figs. 1 and S2 are processed in this way, as are all the supplementary movies.

Each raw image, denoted $I_{\text{raw}}$, is processed according to the following steps: First, a dark image, $I_{\text{dark}}$, is acquired by taking the time-median of many frames (200 frames for 100 Hz data and 2,000 for 1,000 Hz data) when the illumination beam is blocked. This image is subtracted from each raw image, yielding $I_{\text{bkgd}} = I_{\text{raw}} - I_{\text{dark}}$. Second, features bigger than $\sigma_1 = 1.5$ pixels are removed by subtracting a Gaussian blur, yielding $I_{\text{smooth}} = I_{\text{bkgd}} - \text{blur}(I_{\text{bkgd}}, \sigma_1)$, where $\text{blur}(I, \sigma)$ is a 2D Gaussian blur of the image $I$ using a standard deviation $\sigma$. We choose $\sigma_1 = 1.5$ to minimize intensity changes that arise from time-varying background fringes, even though this choice slightly decreases the normalized intensities of the particles on the coverslip. Third, the image is normalized to the background that has been blurred with $\sigma_2 = 20$ pixels, so that particles on the coverslip and stray fringes smaller than $\sigma_2$ do not affect the normalization. This process yields $I_{\text{norm}} = (I_{\text{smooth}})/\text{blur}(I_{\text{bkgd}}, \sigma_2)$. Because each image is normalized independently of other images in the time-series, fluctuations in the illumination intensity in time do not affect $I_{\text{norm}}$. Finally, all remaining static features in the background are removed by subtracting the time-median of many frames (300 frames for 100 Hz data and 3,000 for 1,000 Hz data) of the movie, yielding the final processed image $I_{\text{final}} = I_{\text{norm}} - I_{\text{norm,med}}$. The noise in $I_{\text{final}}$ is set by shot noise for the first few seconds after the background subtraction, but after this time, fluctuations in the background intensity due to uncorrected mechanical drift are the main source of measurement noise.

**Identifying and measuring assembling particles.** To identify assembling particles, we manually locate the centers of all dark spots that appear and are between 1 and 4 pixels across in each processed interferometric scattering movie. We repeat this procedure multiple times using different frames for the background subtraction to ensure that no dark spots are missed. For each of these spots, we measure the mean intensity in a circle of radius 1 pixel that is centered on the particle as a function of time.

We reject any spot that (1) instantaneously appears in the movie, indicating that it is from a particle that has adsorbed to the coverslip; (2) is near the gold particle used for active stabilization or near a defect on the coverslip that has comparable intensity (greater than 0.1); (3) is near a particle that adsorbs to or desorbs from the coverslip, such that its intensity is altered by the particle; (4) is so close to another spot that the interference fringes of the two spots overlap; (5) is near the edge of the field of view; or (6) grows at a slow and consistent rate over the course of the measurement, consistent with protein assembly in the absence of RNA. We describe how each of these criteria are applied below.

The spots from particles that adsorb to the coverslip are easily identified because they appear instantaneously in one frame of the movie instead of gradually appearing over the course of many frames. In some cases, such particles can be seen approaching the coverslip before adsorption.

Spots within 8 pixels of the gold particle used for active stabilization or a bright defect on the coverslip are rejected. There are typically fewer than 2 defects on the coverslip in a given field of view. The spots that grow near the gold particle or defect are not analyzed because they may be due to growth that occurs on the gold particle or defect instead of on the RNA.

Furthermore, the in-plane active stabilization keeps the coverslip position constant to within only a few nanometers, and when particles as bright as the gold particles move by a few nanometers they produce intensity changes that are similar to or larger than the intensity of an MS2 capsid. These intensity changes affect the measured intensity of any nearby assembling particles.

To determine if a spot is near a particle that adsorbs to or desorbs from the coverslip, we check if the interference fringes of an absorbing or desorbing particle overlap with the spot at any point during the movie. If they do, we examine the intensity of the particle as a function of time to check if there is an abrupt change in intensity that occurs on the same frame as the adsorption or desorption event. If the abrupt change in intensity is greater than 0.0003 (10% of the intensity of a capsid), we reject the spot for analysis. By not analyzing these spots, we avoid misinterpreting intensity changes that are due to the adsorption or desorption event as features of the assembly kinetics.

A spot is determined to be too close to another spot if their centers are within 4 pixels of each other. If two spots are closer than this distance, their interference fringes overlap, and the measured intensity of each will depend on the intensity of the other.

Similarly, we do not analyze any spot with a center that is within 4 pixels of the edge of the field of view. We do not analyze these spots because the interference patterns for the spot are not fully visible, and we cannot determine if there are particles beyond the edge of the field of view that affect the spot's intensity.

Finally, we do not analyze spots that grow slowly and synchronously with a consistent growth rate over the course of the measurement (Fig. S3). In a typical experiment, we observe 1–10 of these spots (Supplementary Movie 1). We observe a similar number of spots with similar growth kinetics in control experiments where RNA is not added to the surface (Supplementary Movie 5). We therefore conclude that these spots likely do *not* represent the assembly of coat-protein dimers around RNA. They may represent protein aggregates growing on the coverslip surface.

**Determining start and growth times.** The cumulative distribution functions of the start times before assembly (Figs. 2 and S5) are measured as follows. Each start time is defined as the time at which a kinetic trace reaches an intensity of 0.001. To measure this time, we smooth each trace using a 1,000-frame moving average. The first time that the smoothed trace reaches an intensity greater than 0.001 is called $t_1$, and the last time that the smoothed trace has an intensity less than 0.001 is called $t_2$ (ignoring any late detachment events or drifts in intensity). The start time is then determined as $t_{start} = (t_1 + t_2)/2$. To estimate the uncertainty in each start time, we calculate the half-width of the moving-average window and $(t_2 - t_1)/2$, and we take the greater of the two. Note that this uncertainty does *not* account for stochastic variations inherent in counting a finite number of discrete events, but we account for such variations by comparing the results from repeated experiments, as described below.

For each experiment, we fit the cumulative distribution of measured start times to the exponential function

$$N(t) = A \left(1 - \exp\left[-(t - t_0)/\tau\right]\right) \tag{1}$$

using a Bayesian parameter-estimation framework with fit parameters $A$, $t_0$, and $\tau$. A uniform, unbounded prior is used for all parameters. Note that we must fit for the saturation value of the exponential $A$ because we do not know *a priori* the number of RNA molecules tethered to the surface in our field of view, or if additional particles assemble after we stop recording images. To perform the fit we first invert the exponential function, yielding

$$t(N) = t_0 - \tau \ln\left(1 - N/A\right). \tag{2}$$

The posterior probability distribution $p(t_0, A, \tau \mid D_{CDF}, M)$, where $D_{CDF}$ is the observed cumulative distribution function and $M$ is the model (Equation (2)), is then sampled using an affine-invariant ensemble Markov-chain Monte Carlo sampler (11) with 50 walkers that take 500 steps each. The walkers are initially distributed in a narrow Gaussian around the peak of the posterior probability density function. The position of the peak is calculated from a least-squares fit to $t(N)$. The walkers reach an equilibrium distribution after approximately 200 steps. Pair plots of the positions of the walkers on every step after the burn-in are shown in Fig. S5, along with the marginal distributions for each fit parameter. The best-fit parameters reported in the text are taken as the $50^{th}$ percentile of the marginal distributions, and the reported uncertainties represent the standard deviation in the best-fit parameters from repeated experiments.

To determine the growth time we first take the portion of each kinetic trace that lies between the start time and the time at which the intensity first reaches the $10^{th}$ percentile of the capsid intensity distribution (Fig. S2), and fit this portion of the trace to a line using a least-squares method. We then estimate the time required to grow a full capsid (bind 90 dimers) by approximating the growth rate as the slope of the linear fit.

**TEM of assembled particles.** We use negative staining and TEM to image the protein structures that form on MS2 RNA. First, we describe assembly experiments with MS2 RNA that is tethered to the surface of 30-nm gold particles (Figs. 2e and S4). The surfaces of the gold particles are functionalized in a way that is similar to that used for the coverslips. The protocol is identical to that used to prepare the gold tracer particles for active stabilization, except that we use NHS-PEG-N$_3$ instead of NHS-PEG. To conjugate DNA oligonucleotides to the PEG-coated gold particles, we add 5 μM DBCO-DNA to 10 nM gold particles in PBS without Ca or Mg. The mixture is left at room temperature overnight in a tube rotator and then washed 5 times by centrifuging the mixture at 8,000 g for 5 min and resuspending in TE buffer.

To perform the assembly reaction, we add a 100-fold molar excess of RNA-DNA complexes (20 nM) to the gold particles (0.2 nM) and equilibrate the mixture in TNE buffer for 1 hr on ice. We then take 6 μL of this mixture, add 0.42 μL of 30 μM

coat-protein dimers suspended in 20 mM acetic acid, and let the mixture sit for 10 min at room temperature. The mixture is then added to a plasma-etched carbon-coated TEM gird (Ted Pella), left to sit for 1 min, and then removed by blotting with filter paper. Then 6 µL of methylamine tungstate stain solution (Nanoprobes) are added and left to sit for 1 min before removal by blotting with filter paper. We visualize the samples on a Tecnai F20 (FEI) transmission electron microscope operated at 120 kV. Images are captured on a 4,096 × 4,096-pixel CCD camera (Gatan). Representative images are shown in Fig. S4 along with images of control reactions involving bare RNA without the DNA linkage.

We also perform assembly reactions with RNA that is free in solution. This is done by mixing varying concentrations of coat protein with 10 nM of RNA in assembly buffer. After allowing the assembly reaction to proceed for a fixed amount of time, the mixture is imaged by TEM, as described above. Representative electron micrographs of particles assembled with 1.5, 2, and 4 µM coat-protein dimers are shown in Fig. S8.

## Additional control experiments

**Lower illumination intensity.** To test whether the intensity of the incident beam affects the assembly process, we perform a set of duplicate control experiments with 2 µM coat-protein dimers and a light intensity that is 10-fold smaller (approximately $0.3\ \mathrm{kW/cm^2}$). The results, shown in Fig. S14, are similar to those of the higher-intensity experiment presented in Figs. 2, S1, and S5. Again, different assembling particles appear after different start times. The cumulative distribution function of the start times is well-fit by the same exponential function but with best-fit parameters $t_0 = 62$, $A = 39$, and $\tau = 49$ for the first control experiment of the duplicate set, and $t_0 = 148$, $A = 39$, and $\tau = 159$ for the second control experiment (the posterior probability distributions for the fit parameters are shown in Fig. S14b). 24 out of 39 traces plateau at intensities consistent with that of a full capsid, 2 plateau at smaller intensities, and 13 plateau at larger intensities in the first control experiment, while 25 out of 36 traces plateau at intensities consistent with that of a full capsid, 5 plateau at smaller intensities, and 6 plateau at larger intensities in the second experiment. These fractions are similar to those observed in the 2 µM experiment presented in the main text.

The results of the control experiments indicate that the incident light does not qualitatively affect the assembly process. The observed kinetic traces and distribution of start times are consistent with those expected from a nucleation-and-growth process. Moreover, because the difference between identically performed low-intensity control experiments is larger than those between the high-intensity experiments and either of the controls, we conclude that other factors, such as differences in the concentration of protein, are responsible for the variation. Indeed, the variation in both the fitted time constants $\tau$ and the delay times $t_0$ among different experiments is not unexpected, given the strong dependence of the start times on concentration. At 1 µM protein concentration, all the start times are longer than the 600-s duration of the experiment, so that even a slight difference in the flow profile of the injected protein solution during the 2 µM experiments could cause the 110-s spread between the measured time constants and the 86-s spread in the delay times.

**RNA-coverslip binding.** We perform two experiments to explore how the MS2 RNA interacts with the DNA coated coverslips. With one experiment we investigate how the RNA-DNA complexes initially bind the coverslip, and with the other we investigate how the RNA and coverslip interact after the initial binding.

We test how the RNA-DNA complexes bind to the coverslip by injecting solutions containing 1 nM of either bare RNA or RNA-DNA complexes in hybridization buffer into the imaging chamber of the interferometric scattering microscope. If the binding is specific and is due to the DNA linkage, we expect only the RNA-DNA complexes to stick to the coverslip surface. The bare RNA is injected first, and we image the system for 60 s to detect each molecule that binds. We then inject the RNA-DNA complexes, and we repeat the measurement. The location of each detected binding event is shown in Fig. S16a. We observe a total of 3 bare RNA molecules and 47 RNA-DNA complexes. We conclude that the binding between the RNA-DNA complexes and the coverslip is highly specific, and that most of the RNA-DNA complexes that are bound to the coverslip are tethered by a DNA linkage.

Having established that the initial binding of RNA to the coverslip occurs by the RNA-DNA linkage, we must now rule out the possibility that nonspecific interactions between the tethered RNA and the nearby coverslip surface might lead to the observed energy barrier to assembly. If such interactions exist, they might cause the RNA to adhere partially to the coverslip, making it inaccessible to coat proteins. Thus, the energy barrier we measure could be the barrier associated with lifting the RNA from the surface such that it is accessible to coat proteins. For this scenario to describe our observations, the coat proteins must also help lift the RNA from the surface, since the measured start times depend strongly on the concentration of coat protein. We can test for this type of barrier by severing the DNA linkage and measuring how long the RNA stays bound to the coverslip. If the time required for the RNA to detach from the surface is less than the start times we measure in assembly at the lowest coat protein concentration, we can conclude that any nonspecific binding of the RNA to the coverslip does not significantly affect the barrier to assembly.

We sever the DNA linkage using toehold mediated strand displacement (12). We use a different linker oligonucleotide (linker 2) to attach the RNA to the coverslip. Linker 2 is identical to the linker we use for assembly experiments except that it has 6 additional bases at its 3′ end. Its sequence is 5′-CGACAGGAAGTTGAGCAGGACCCCGAAAGGGGTCCCACCCCCCACA CCACAACCCAAACCC**ACACAC**-3′, with the additional bases in bold. When bound to the surface oligonucleotide, these additional bases provide a toehold (12) for a displacer oligonucleotide that is perfectly complementary to linker 2. Owing to this toehold, the displacer can rapidly hybridize to linker 2 (12), displace the surface oligonucleotide, and sever the RNA-DNA linkage.

We estimate how long the RNA remains bound to the coverslip after severing the linkage as follows. We first bind RNA-DNA complexes to the surface using linker 2, and rinse out any unbound RNA using the procedure described below in Assembly experiments. Then, we use the interferometric scattering microscope to estimate the rate at which RNA molecules detach from the surface in the absence of the displacer. We find that 3 particles detach in 60 s. Next, we inject a 10 μM solution of the displacer strand in assembly buffer and measure the detachment rate. We observe that over 100 particles detach from the coverslip within 60 s, confirming that the displacer is capable of severing the DNA linkage and releasing the RNA from the coverslip. The cumulative distribution of RNA detachment times is shown in Fig. S16b.

Because the distribution of RNA detachment times is narrower than the distribution of start times observed in assembly experiments with low protein concentrations, we conclude that the observed energy barrier to assembly does not result from RNA-coverslip interactions. To determine the characteristic RNA detachment time $\tau_{\mathrm{det}}$, we fit an exponential function to the cumulative distribution of detachment times using the Bayesian parameter estimation method described above. We find that the exponential function fits the observed detachment times well (Fig. S16b), with best-fit parameters of $A_{\mathrm{det}} = 134.2 \pm 0.2$, $t_{0,\mathrm{det}} = 10.0 \pm 0.2$ s, and $\tau_{\mathrm{det}} = 9.36 \pm 0.03$ s, where the uncertainty represents the 16th and 84th percentiles of the posterior probability distributions. The roughly 10-s characteristic detachment time is consistent with the time required for the displacer oligonucleotides to diffuse to the surface and the displacement reaction to occur (12). Moreover, the detachment timescales are about an order of magnitude lower than the start times in assembly experiments with 1.5 and 2 μM of coat-protein dimers. Thus, our measured distribution of assembly start times does not likely result from RNA-coverslip interactions that make the RNA inaccessible to coat proteins.

## Estimating timescales

**Time for protein to reach the surface-bound RNA.** Here we estimate how long it takes MS2 coat-protein dimers to reach the surface-bound RNA molecules after the protein is pumped into the imaging chamber. This timescale is set by the rate of diffusion and the distance between the protein and coverglass when it is first introduced.

We first model how fluid is introduced into the imaging chamber. Downstream of the inlet cup, the flow cell contains a cylindrical inlet chamber (1 mm diameter, 3 mm long), which is followed by the imaging chamber (0.75 mm tall, 1.0 mm wide, and 4.6 mm long) that contains our field of view. The field of view is in the center of the bottom surface of the imaging chamber. To simplify our calculations, we assume that the flow cell consists of a single cylindrical chamber with a radius $R = 0.375$ mm and that our field of view is $L = 9.3$ mm from the entrance to the cylinder. The diameter of the cylinder is chosen to match the height of the imaging chamber, and the length $L$ is chosen so that the volume $\pi L R^2$ is the same as the total volume in the actual inlet and imaging chambers upstream of the field of view.

We assume a no-slip boundary condition, such that the flow profile in the model cylindrical chamber is laminar and parabolic (13). In our experiments, we inject $V = 10$ μL of fluid over 20 s, so that the average flow velocity is approximately 0.5 mm/s, yielding a Reynolds number of 0.5, which justifies the laminar assumption. We further assume that the diffusion of protein across the chamber is negligible over the duration of the pumping, so that the parabolic front that separates the new protein solution from the old buffer solution is sharply defined. Indeed, the time for an MS2 coat-protein dimer (hydrodynamic radius 2.5 nm (Ref. 3) with diffusion coefficient, $D = 90$ μm²/s) to diffuse across the cylinder radius is approximately 1,600 s, much larger than the pumping duration. The shape of the parabolic boundary is described by $x(r) = \left(2V/\pi R^2\right)\left(1 - (r/R)^2\right)$, where $r$ is the radial coordinate of the cylinder, and $x(r)$ is the distance down the cylinder from the end where the protein is injected (Fig. S7). Note that in the center of the cylinder, $x(r = 0) \approx 45$ mm. Thus, the tip of the parabola following a pump of V = 10 μL extends well beyond the field of view. Above the field of view, the distance from the parabolic boundary to the surface is $a = R(1 - \sqrt{1 - \pi R^2 L/2V}) \approx 40$ μm. This is the distance that the protein must diffuse to reach the surface-bound RNA.

To experimentally determine the distance from the parabolic boundary to the surface just after the pump, we use a bright-field microscope (Eclipse Ti, Nikon) and tracer particles (1 μm sulfate-latex, Invitrogen). For this experiment we fill the flow cell with water, position our field of view in the center of the imaging chamber, inject a solution of tracer particles (0.08% w/v in water), and measure the distance of the tracer particles from the coverslip immediately after the injection. We find that there is a well-defined boundary between the solutions with and without particles, and that this boundary is $a = 20$–50 μm above the coverslip, depending on the pump and flow cell used. This distance agrees well with the distance calculated above (40 μm).

With this length scale and the diffusion coefficient, we can calculate the time it takes proteins to diffuse to the surface, $t_{\mathrm{D}} = a^2/D$. More specifically, at a distance $a$ from the protein solution, $t_{\mathrm{D}}$ is the time it takes for the concentration of proteins to reach approximately half the injected concentration. For a 20–50 μm distance, we fnd that $t_{\mathrm{D}} = 5$–30 s.

This timescale agrees with the measured delay time that precedes assembly in our experiments. For our assembly experiments, we stop pumping 24 s after the time-series begins, so the concentration of protein at the surface should reach half of the injected concentration about 30–55 s after the beginning of the time-series. Since we do not observe assembly on our experimental timescales when introducing 1 μM protein dimers (Fig. S6), we do not expect to detect assembling particles until after the concentration of dimers at the surface exceeds 1 μM. Thus, when introducing 1.5 μM dimers, we do not expect to detect assembling particles until after this 30–55 s delay, which is indeed the case (Fig. S5). Also, when introducing 2 μM and 4 μM protein dimers, we expect to detect assembling particles a bit sooner but not before this 30–55 s delay, which is again what we observe (Fig. S5).

**Rees F. Garmann, Aaron M. Goldfain, and Vinothan N. Manoharan**

**Protein-RNA collision rate.** Here we use a simple model ([14]) of diffusion to capture to estimate the time required for 90 diffusing coat-protein dimers to collide with the viral RNA. In this model the rate of collisions between diffusing proteins and a spherical target is $R = 4\pi r_\mathrm{t} c_\mathrm{p} D$ where $r_\mathrm{t}$ is the target radius, $c_\mathrm{p}$ is the bulk concentration of protein, and $D$ is the diffusion coefficient of the protein. Thus, the time required for 90 proteins to collide with the target is $t_{90} = 90/R$. Assuming the RNA molecule has a radius of $r_\mathrm{t} = 10$ nm, the coat-protein dimers have a diffusion coefficient of $D = 90$ $\mu\mathrm{m}^2/\mathrm{s}$ ([3]), and the concentration of protein dimers is $c_\mathrm{p} = 1$ $\mu$M, then we expect 90 dimers to collide with the RNA within $t_{90} \approx 10$ ms. Thus, the time required for 90 coat-protein dimers to collide with the RNA is roughly 4 orders of magnitude smaller than the median growth time at 2 $\mu$M coat-protein dimers.
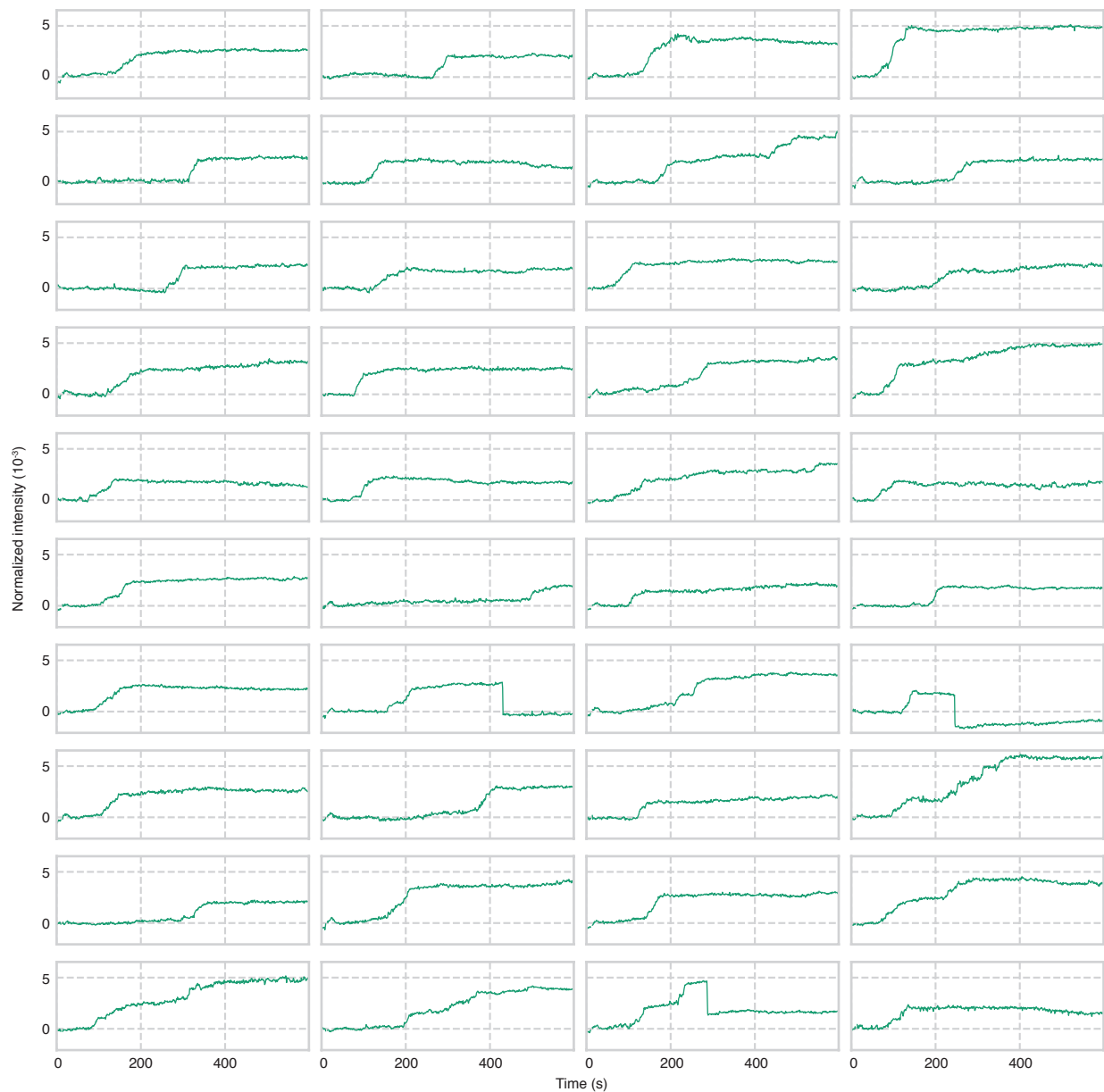
**Fig. S1.** Assembly of 2 μM coat-protein dimers. Traces for 40 of 56 assembling particles in one experiment (corresponding to Supplementary Movie 1) are shown. We interpret the abrupt drops in intensity as detachments. In one trace, the intensity drops to around -0.001, approximately the negative intensity of the RNA in the background image. We interpret this event as detachment of the RNA and assembled proteins from the surface. One trace drops to an intensity near 0, suggesting that the assembled protein detaches from the RNA, which remains on the surface. The intensity of one trace decreases from 0.005 by an amount (0.0032) corresponding to a full capsid, suggesting that overgrown particles can contain capsids. Some of these traces appear in Fig. 2, and one appears in Fig. 1d. The final intensities are used for Fig. 3c. Data are recorded at 1,000 Hz and are plotted with a 1,000-frame average.

**Rees F. Garmann, Aaron M. Goldfain, and Vinothan N. Manoharan**
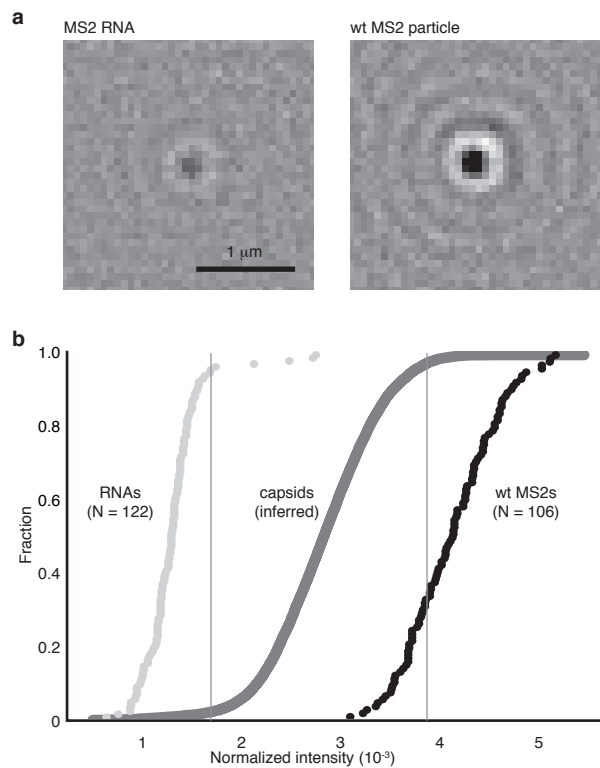
**Fig. S2.** Cumulative distribution of the normalized intensities of MS2 RNA strands and wild-type MS2 virus particles measured in the interferometric scattering microscope. See Supplementary Text for details of the measurement. (a) Images of a single MS2 RNA strand (left) and a single wild-type MS2 virus particle (right). Both images are recorded at 100 Hz and shown with a 300-frame average. (b) We infer the cumulative distribution of intensities for MS2 capsids that fully assemble on surface-tethered RNA by convolving the intensity distribution of the wild-type MS2 particles with the negative of the intensity distribution of the MS2 RNA strands. The gray lines, which mark where the capsid distribution reaches 2.3% and 97.7%, denote the interval we use to identify full capsids in the kinetic traces.
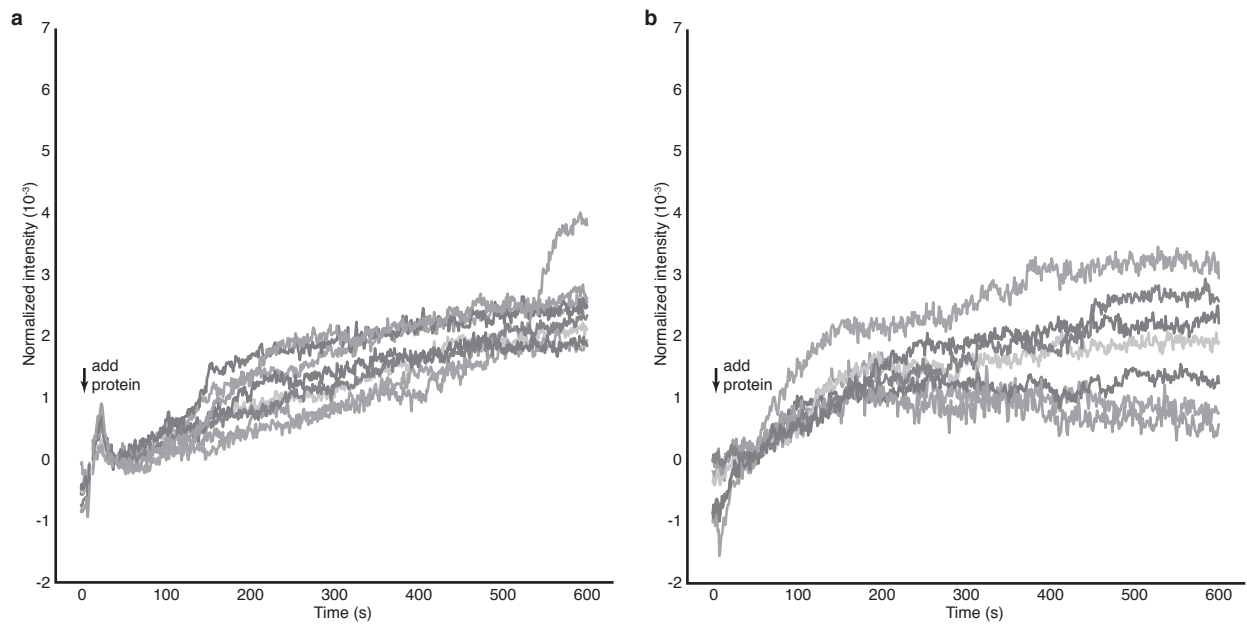
**Fig. S3.** Some of the spots that appear in assembly experiments do not represent assembly around RNA. (a) In the assembly experiment from the main text where we use 2 $\mu$M coat-protein dimers, we observe 8 spots (in addition to the 56 assembling particles described in the text) that grow slowly and synchronously and that show a consistent growth rate over the course of the measurement. The traces of these particles are shown in the plot, which is a 1,000-frame average of the intensities measured from Supplementary Movie 1, recorded at 1,000 Hz. (b) In a control experiment with 2 $\mu$M dimers but no RNA on the surface, we observe 7 spots that grow slowly and synchronously, with traces similar to those shown in panel (a). For this experiment, we bound the linker oligonucleotides to the surface oligonucleotides, but we did not add the RNA. The traces are measured from the data in Supplementary Movie 5. The data is recorded at 1,000 Hz and is plotted with a 1,000-frame average.

**Rees F. Garmann, Aaron M. Goldfain, and Vinothan N. Manoharan**
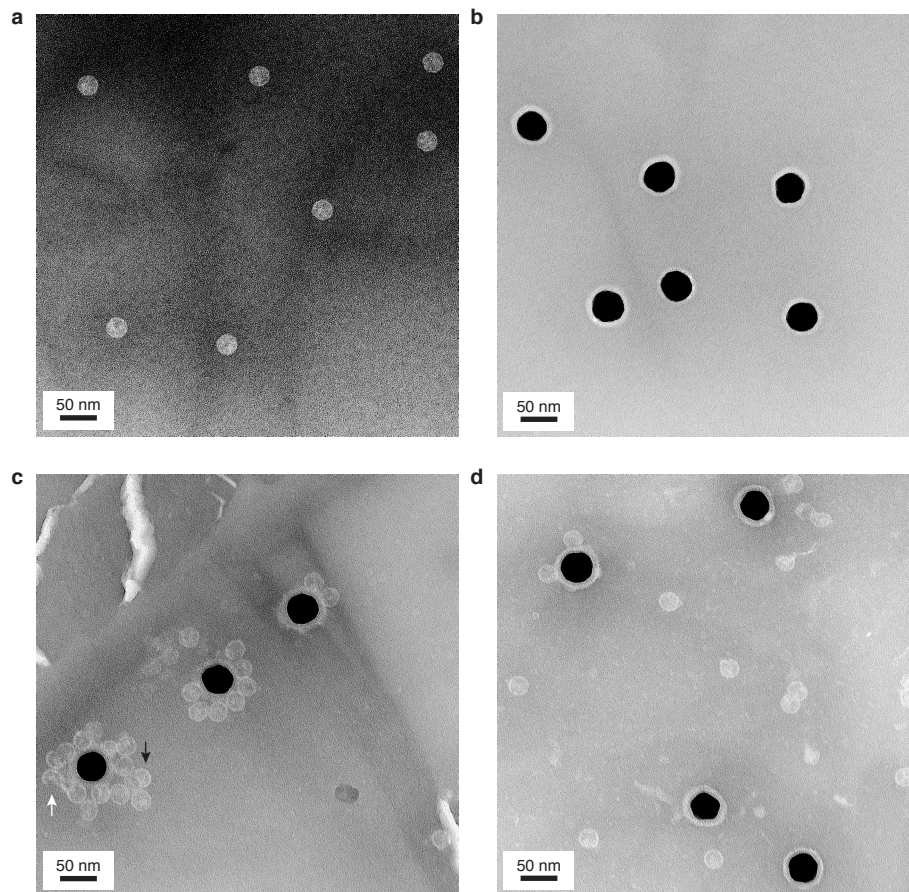
**Fig. S4.** Negatively stained transmission electron micrographs of virus particles, functionalized gold nanoparticles, capsids assembled around RNA strands that are bound to the surface of the gold particles, and capsids assembled around untethered RNA. Each sample is stained with methylamine tungstate stain solution (Nanoprobes) before imaging. (a) Wild-type MS2 particles. (b) Amine-functionalized 30-nm gold nanoparticles (Nanopartz) that are coated with PEG and decorated with surface oligonucleotides. The dark spots are the gold particles, and the surrounding lighter halos are the negatively stained coatings on the particle surfaces. These coatings consist of a proprietary polymer base layer, which is applied by the manufacturer to the gold nanoparticles, and the PEG-DNA molecules that we conjugate to the particles. (c) An assembly reaction in which 2 $\mu$M coat-protein dimers in assembly buffer is added to RNA-DNA complexes that have been incubated for 1 h with the functionalized gold particles. White arrow points to a partial capsid. Black arrow points to a particle that is larger than a capsid. (d) A control reaction in which 2 $\mu$M coat-protein dimers in assembly buffer is added to bare RNA that has been incubated for 1 h with the functionalized gold particles. The higher number of capsids near the surface of the gold particles for the experiments using RNA-DNA complexes suggests that these capsids assembled around RNA-DNA complexes that were tethered to the particle surface.
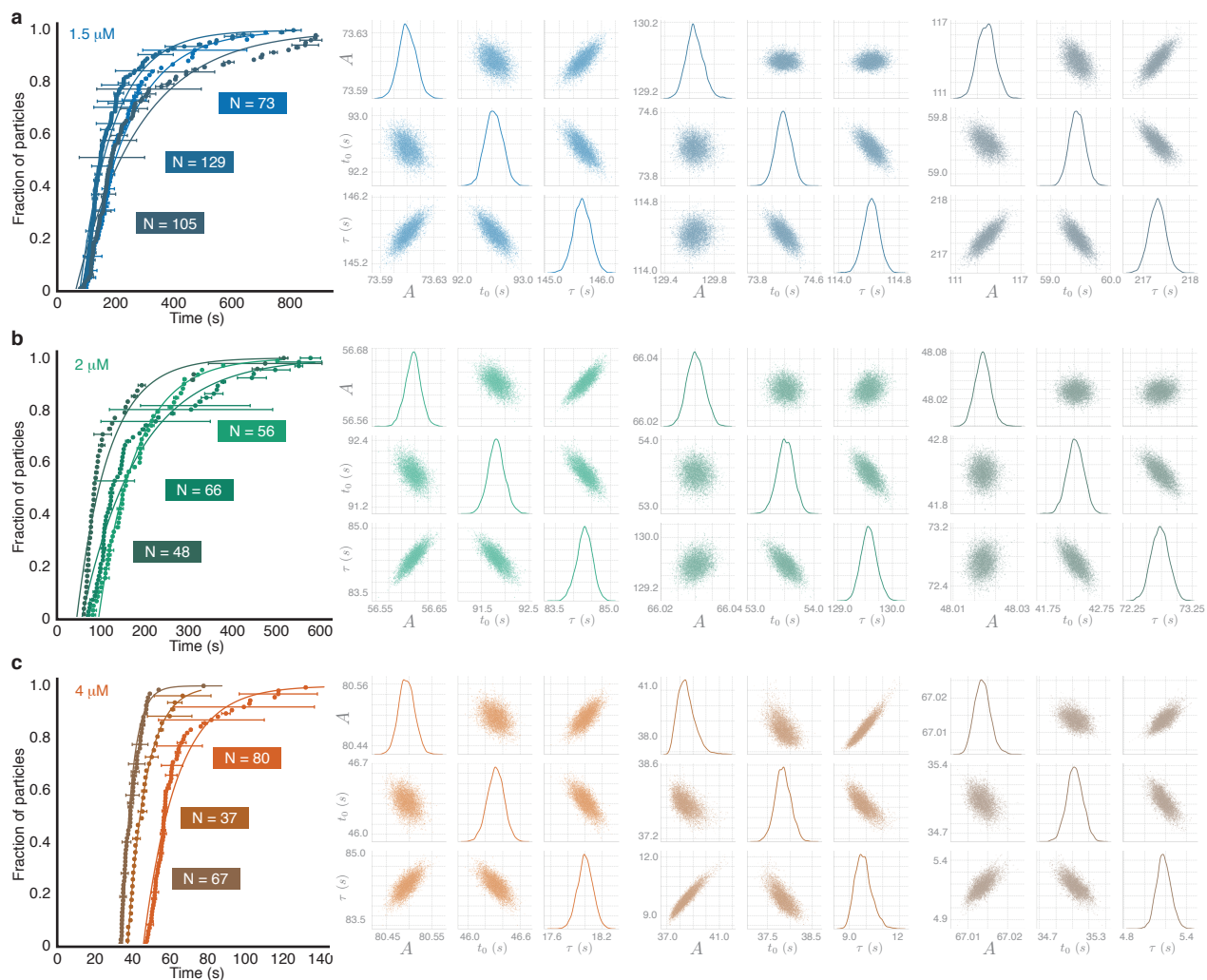
**Fig. S5.** Cumulative distributions of start times and posterior probability distributions of parameter values obtained by fitting the distributions. The results from triplicate assembly experiments with (a) 1.5, (b) 2, and (c) 4 µM dimers are shown. Each cumulative distribution of start times (left) is measured from a separate assembly experiment. Uncertainties in the time measurements are represented by horizontal bars. Fits are shown as solid curves. Numbers of particles (N) are shown on the plot. Posterior probability distributions of parameter values (right) are sampled using a Markov-chain Monte Carlo technique. The plots along the diagonal show kernel density estimates of the fully marginalized posterior distributions of each parameter, while the off-diagonal plots show the joint distributions. The data and fit shown in the lightest color of each panel are from the experiments shown in Figs. 2, 3a-c, S9, and S10. Data from all 9 of the experiments in this figure were used to obtain the nucleation times shown in Fig. 3b.
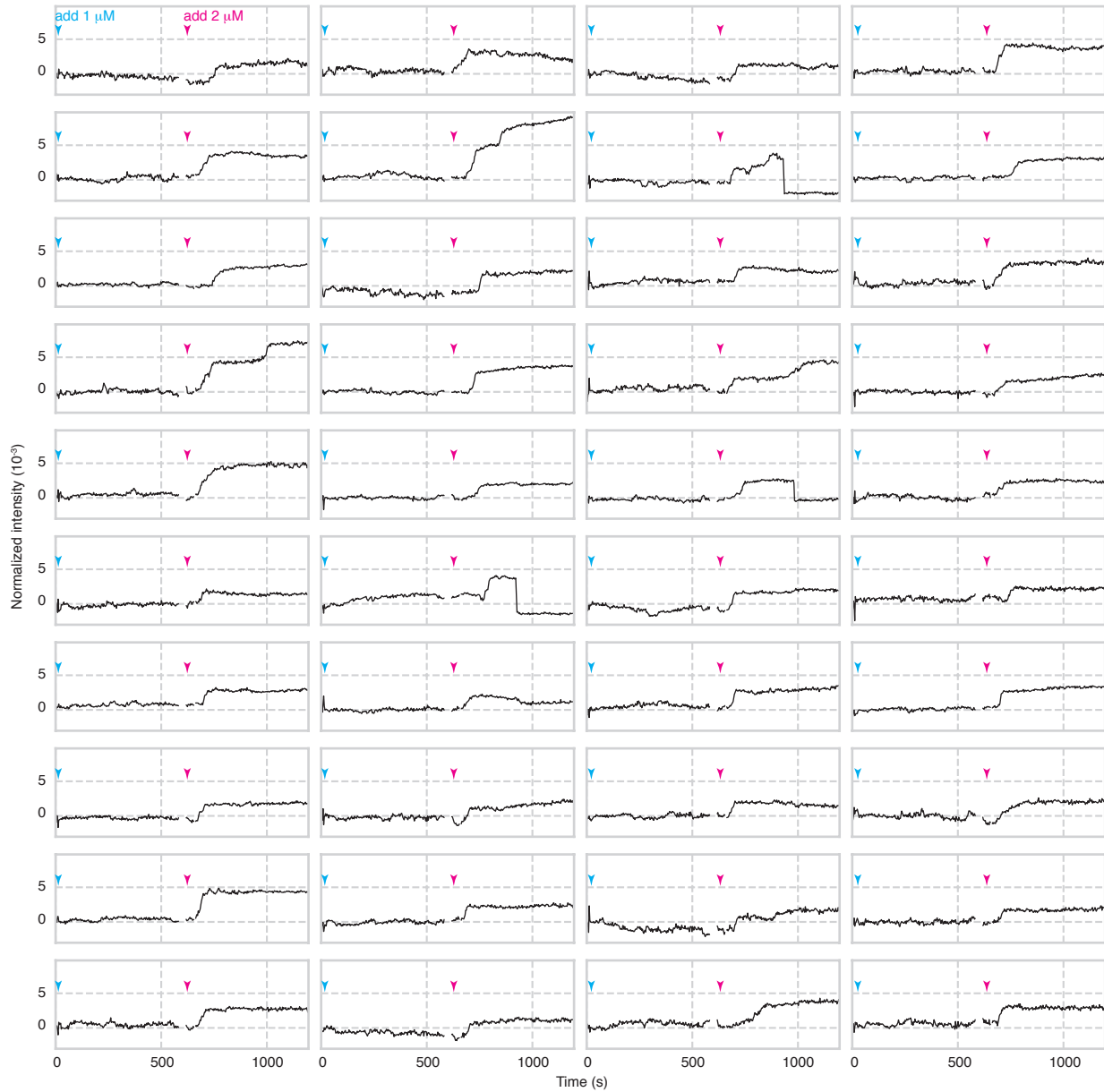
**Fig. S6.** Assembly of 1 μM coat-protein dimers. When 1 μM coat-protein dimers is added (cyan arrowheads) to the surface-bound RNA, no assembling particles appear over the course of 600 s. At this point, 2 μM coat-protein dimers is added (pink arrowheads), after which we observe particles assembling at 75 locations within the field of view. Intensity traces for 40 of these particles are shown above. We also show traces for the first 600 s at the same locations. There is no data between 586 and 615 s, during which time we block the illumination beam and inject the 2 μM protein. As in Fig. S1, we interpret abrupt drops in intensity after assembly as detachment events. The traces are measured from the data shown in Supplementary Movie 2. The data are recorded at 100 Hz and are plotted with a 300-frame average.
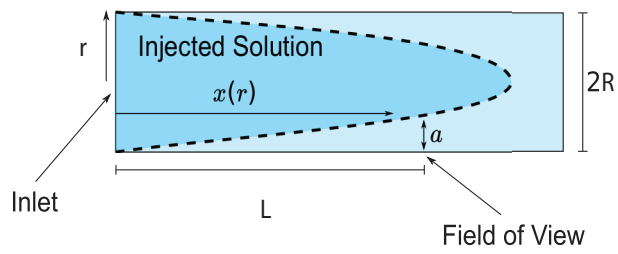
**Fig. S7.** Model of the flow profile for the injected protein. We model the flow chamber as a cylinder, as discussed in the Supplementary Text. The dashed line represents the parabolic boundary between the injected protein solution and the solution that is already in the chamber.
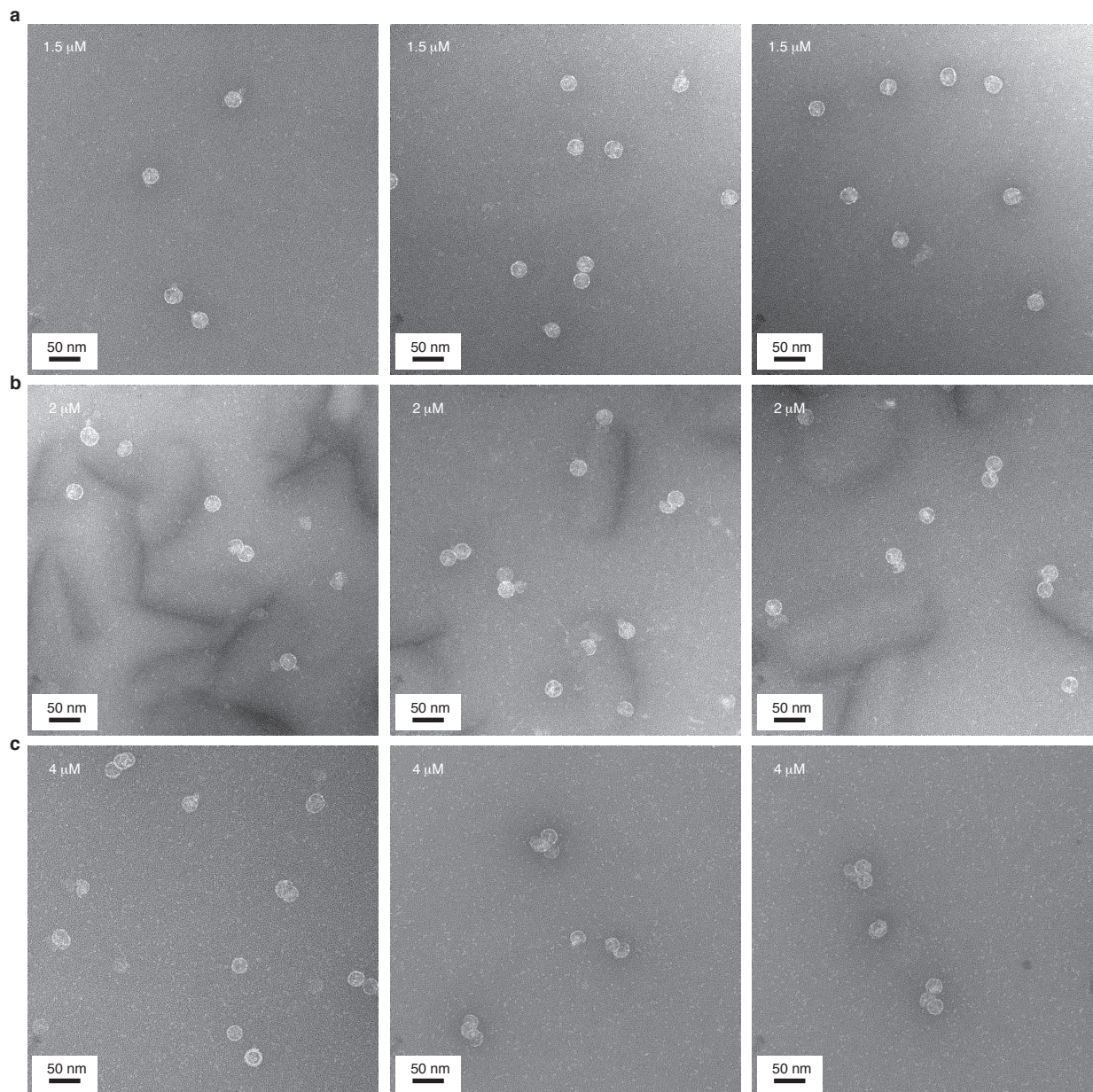
**Rees F. Garmann, Aaron M. Goldfain, and Vinothan N. Manoharan**

**Fig. S8.** Negatively stained transmission electron micrographs of assembled particles from control experiments performed with varying concentrations of protein and untethered RNA. Each sample is stained with methylamine tungstate stain solution (Nanoprobes) before imaging. (a) Three micrographs of particles taken 20 min after mixing 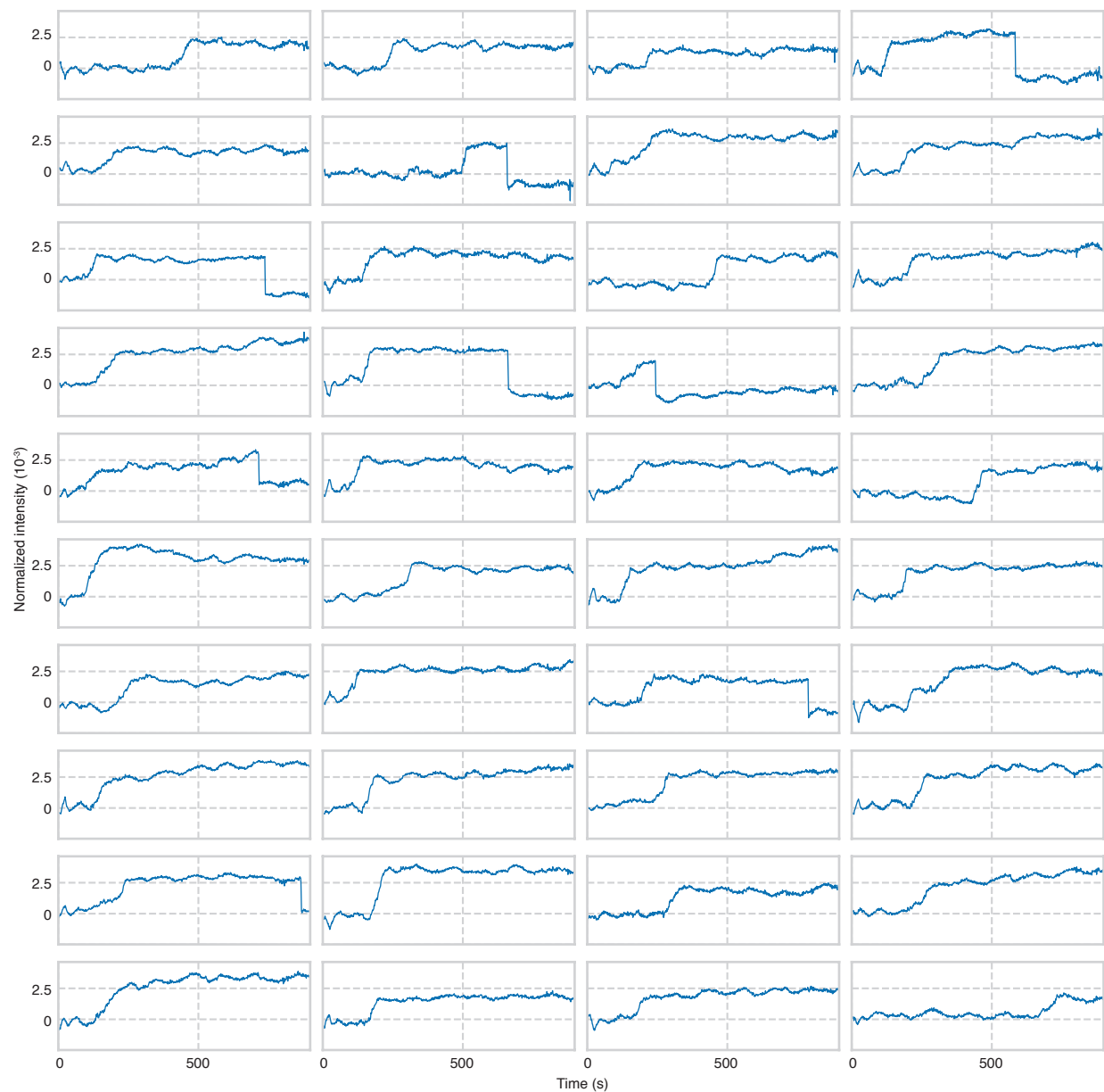1.5 μM coat-protein dimers and 10 nM RNA in assembly buffer. (b) Three micrographs of particles taken 10 min after mixing 2 μM coat-protein dimers and 10 nM RNA in assembly buffer. (c) Three micrographs of particles taken 10 min after mixing 4 μM coat-protein dimers and 10 nM RNA in assembly buffer.
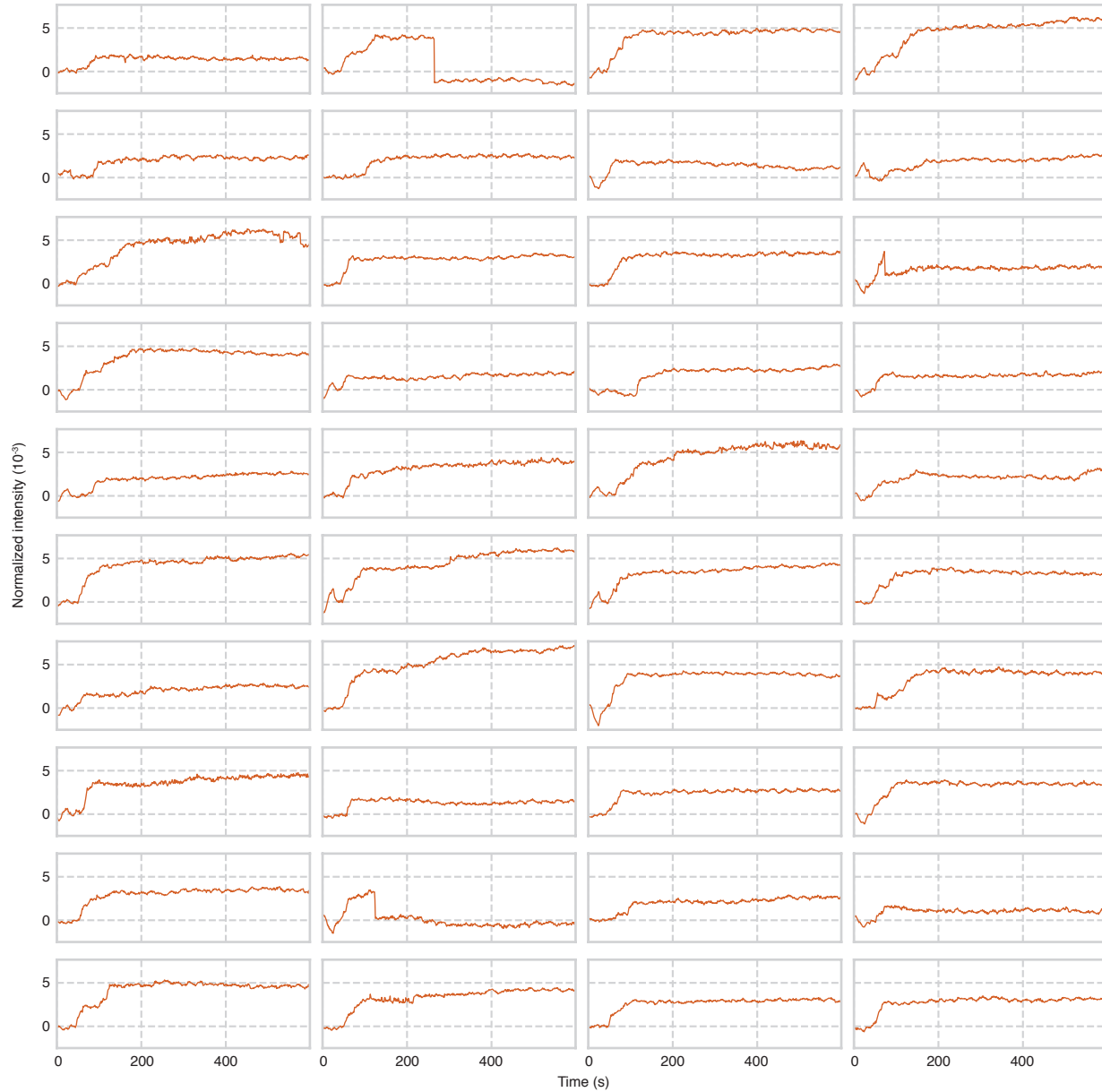
**Fig. S9.** Assembly of 1.5 μM coat-protein dimers. Kinetic traces for 40 of the 73 observed assembling particles in one experiment are shown. As in Fig. S1, we interpret abrupt drops in intensity after assembly as detachment events. A portion of the traces from the same experiment appear in Fig. 3a. The final intensities of the particles in this experiment are used for Fig. 3c. The traces are measured from the data shown in Supplementary Movie 3. The data are recorded at 1,000 Hz and are plotted with a 1,000-frame average.

**Fig. S10.** Assembly with 4 μM coat-protein dimers. Kinetic traces for 40 of the 80 observed assembling particles in one experiment are shown. As in Fig. S1, we interpret abrupt drops in intensity after assembly as detachment events. A portion of the traces from the same experiment appear in Fig. 3a. The final intensities of the particles in this experiment are used for Fig. 3c. The traces are measured from the data shown in Supplementary Movie 4. The data are recorded at 1,000 Hz and are plotted with a 1,000-frame average.
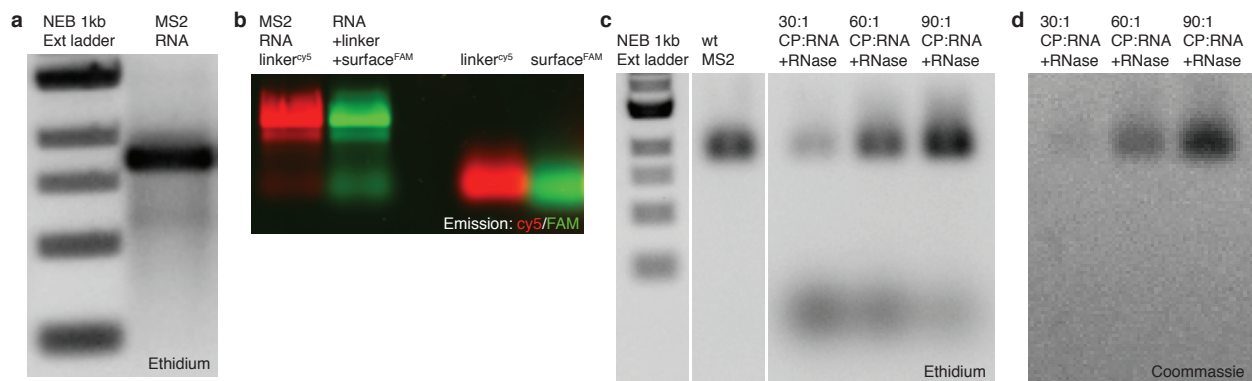
**Fig. S11.** Native agarose gel electrophoresis is used to determine the integrity of the RNA, the yield of RNA-DNA hybridization, and the yield of RNA packaging by MS2 coat protein. All gels consist of 1% agarose in TAE buffer. (a) The MS2 RNA used in the assembly experiments appears as a single band with minimal smearing, indicating that the RNA is not degraded. The left lane contains a 1-kb extended DNA ladder (New England Biolabs), and the right lane contains 1 $\mu$g of MS2 RNA. The gel is visualized after staining with Gel Red (Biotium Inc.) ethidium stain. (b) Fluorescent linker and surface oligonucleotides migrate with the RNA after hybridization and purification, indicating strong specific binding. The leftmost lane is prepared by mixing 1 $\mu$g of MS2 RNA and a 10-fold molar excess of fluorescently labeled (5$'$-cy5) linker oligonucleotide (Integrated DNA Technologies). The RNA is hybridized to the linker by thermal annealing, and the unbound linker is removed by centrifugal filtration. The second-to-leftmost lane is prepared by mixing 1 $\mu$g of MS2 RNA and a 10-fold molar excess of non-fluorescent linker oligonucleotide. The RNA and linker oligonucleotide are hybridized and the unbound linker purified as before. Then a stoichiometric amount of fluorescently labeled (5$'$-FAM) surface oligonucleotide (Integrated DNA Technologies) is added. The second-to-rightmost lane contains free 5$'$-cy5 linker oligonucleotide, and the rightmost contains free 5$'$-FAM surface oligonucleotide. The gel is visualized without staining by imaging the fluorescence emission of the cy5 and FAM dyes on separate channels. (c) MS2 coat-protein dimers (CP) package MS2 RNA into RNase protected complexes with the same mobility as wild-type (wt) MS2 particles. The leftmost lane contains 1-kb extended ladder. The next lane contains wild-type MS2 particles. The next three lanes are prepared by mixing 1 $\mu$g of MS2 RNA and increasing molar ratios of CP in 10 $\mu$L of TNE buffer. The mixtures are incubated for 30 min at room temperature and then treated with 10 ng of RNase A (Amresco Inc.). Electrophoresis is performed 30 min after RNase treatment, and the gel is visualized after staining with ethidium. Protected RNA migrates with the same mobility as wt virus particles, and digested RNA migrates farther down the gel. The amount of digested RNA decreases with increasing CP. (d) Assembling particles prepared and then treated with RNase as just described contain protein, as evidenced by staining with coomassie (Instant Blue) protein stain.
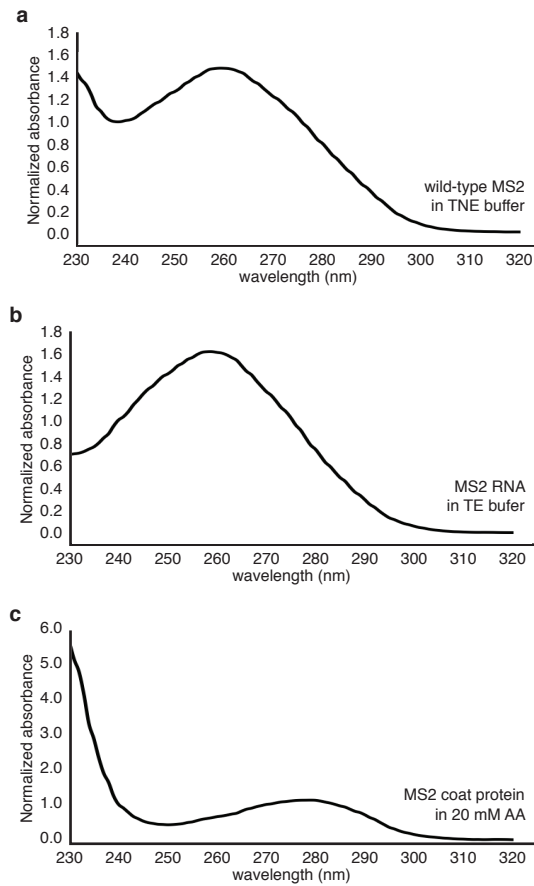
Rees F. Garmann, Aaron M. Goldfain, and Vinothan N. Manoharan

**Fig. S12.** Purities of wild-type MS2 virus, its RNA, and its coat protein are determined by UV-vis spectrophotometry. Absorbance spectra for purified (a) wild-type MS2, (b) MS2 RNA, and (c) MS2 coat protein. The 260/280 ratio of wild-type MS2 in TNE buffer is 1.84, of MS2 RNA in TE buffer is 2.16, and of unassembled coat-protein dimers in 20 mM acetic acid is 0.58. Each spectrum is normalized so that the absorbance is 1.0 at 240 nm. All absorbance measurements are made using a Nanodrop-1000 spectrophotometer (Thermo Scientific).
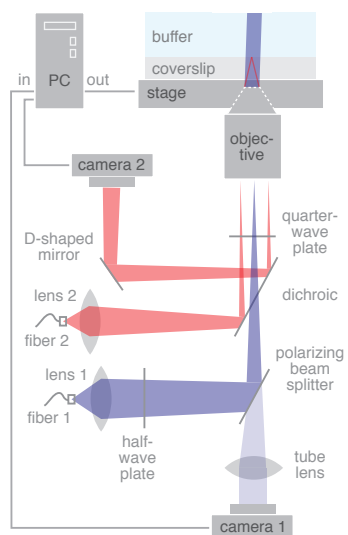
**Fig. S13.** Diagram of the interferometric scattering microscope. Details of the instrument are described in Supplemental Text.

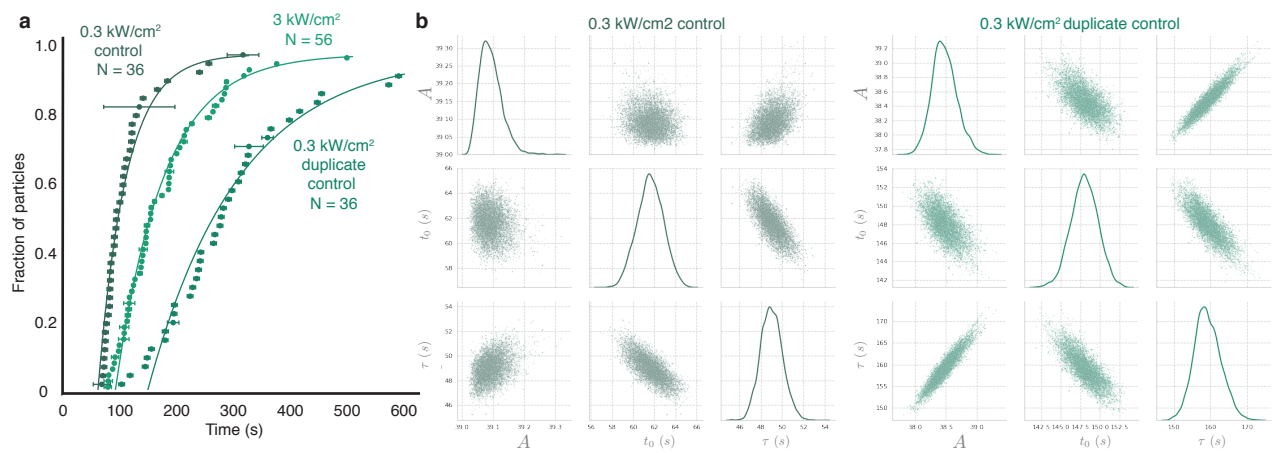Rees F. Garmann, Aaron M. Goldfain, and Vinothan N. Manoharan

**Fig. S14.** Comparison of the nucleation kinetics for assembly experiments performed with 2 μM of coat-protein dimers and different illumination intensities. (a) Cumulative distribution of start times and exponential fits for two low-intensity control experiments and the 2 μM experiment shown in Figure 2. Uncertainties in the time measurements are represented by horizontal bars. Fits are shown as solid curves. Numbers of particles (N) are shown on the plot. (b) Posterior probability distributions of parameter values are sampled using a Markov-chain Monte Carlo technique. The plots along the diagonal show kernel density estimates of the fully marginalized posterior distributions of each parameter, while the off-diagonal plots show the joint distributions.
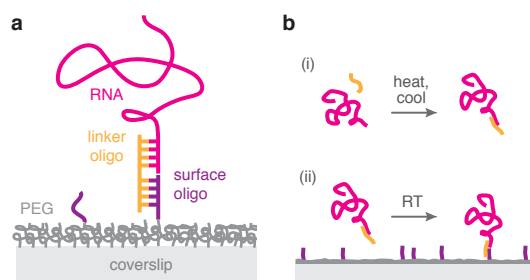
**Fig. S15.** Cartoon of DNA linkages. We use DNA linkages to bind MS2 RNA to the surface of a microscope coverslip. (a) Diagram of the basepairing between the $5'$-end of the RNA, a linker oligonucleotide, and a surface oligonucleotide that is covalently bound to the PEG-functionalized coverslip. (b) To construct the linkages we (i) bind the RNA to the linker oligonucleotide in solution by thermal annealing, and then (ii) add the RNA-DNA complexes to the functionalized coverslips at room temperature. Details of the process are described in Supplemental Text.
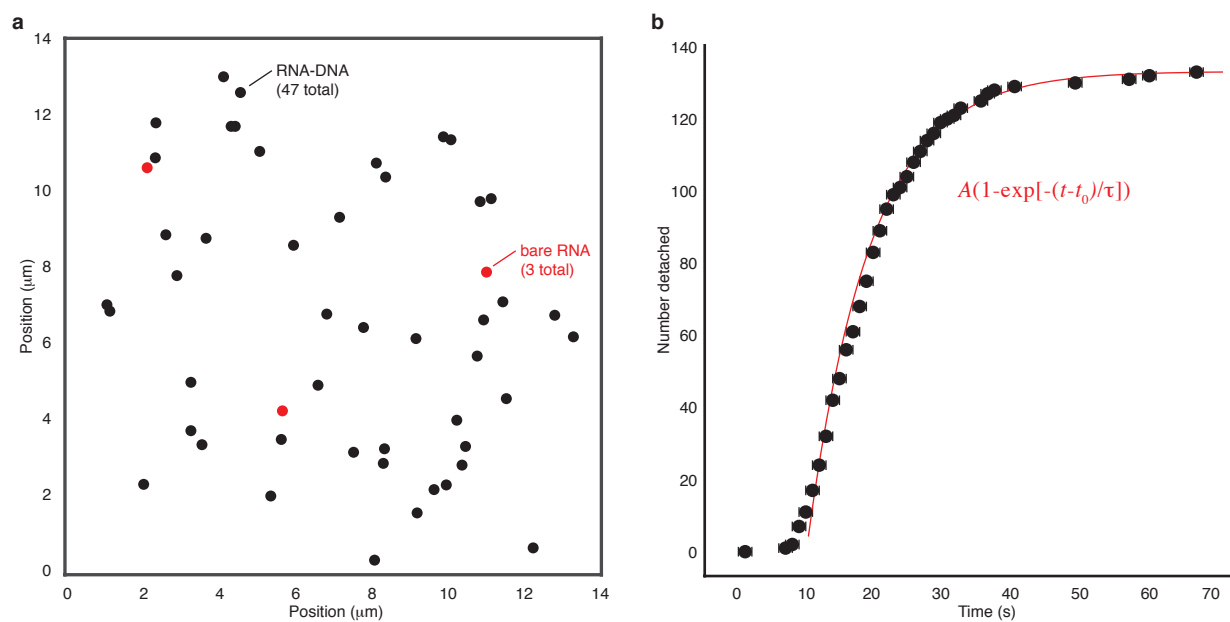
**Rees F. Garmann, Aaron M. Goldfain, and Vinothan N. Manoharan**

**Fig. S16.** Specific binding of RNA to the coverslip via DNA linkages. (a) The locations of bare RNA molecules (red) and RNA-DNA complexes (black) that bind to the coverslip in a 1-min video. See Supplementary Text for details of the experiment. (b) Cumulative distribution of RNA detachment times (points) and an exponential function fit to the data (line) after injecting the DNA displacer oligonucleotide. See Supplementary Text for details of the experiment.
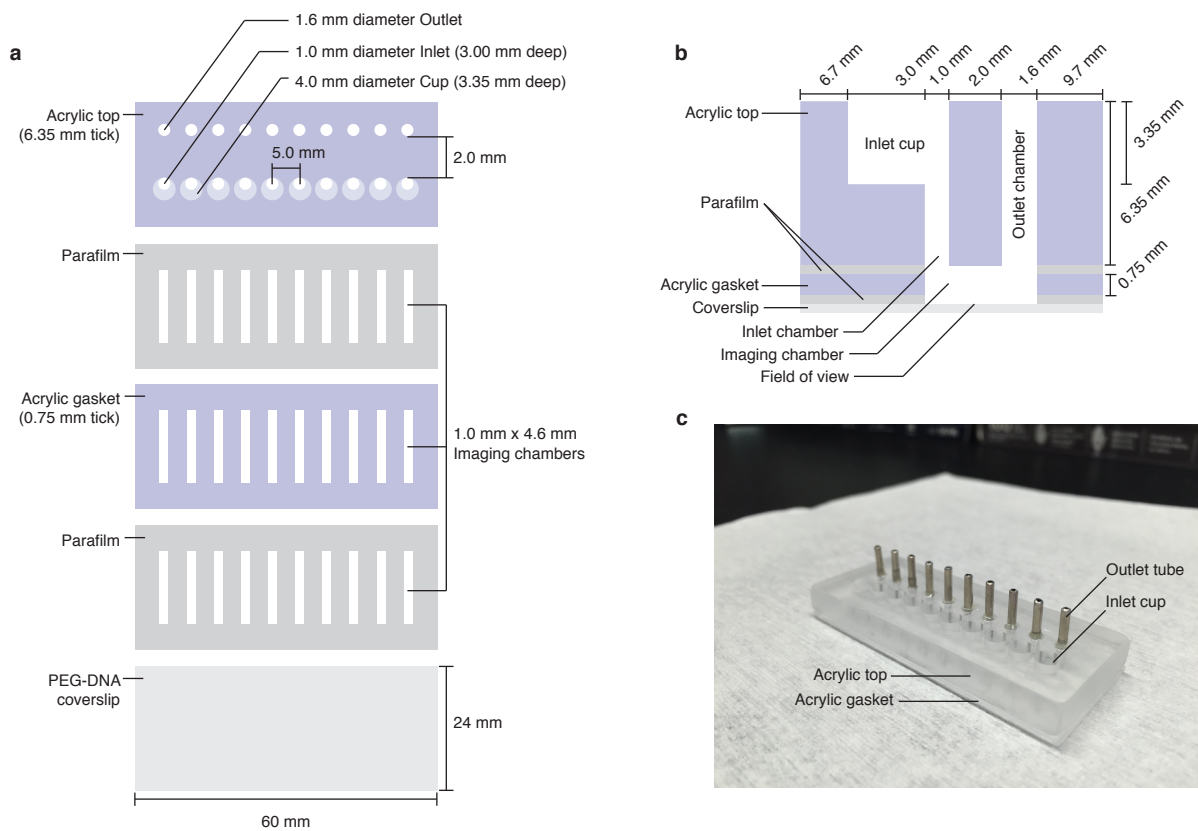
**Fig. S17.** A schematic of the rigid flow cell. (a) Each of the layers used to build the flow cell are stacked on top of one another. When heated, the Parafilm seals the layers together. (b) A cross-section of a flow cell. (c) A photo of an assembled flow cell. Aluminum tubes are epoxied into the outlet chambers to connect to the Tygon tubing.

**Rees F. Garmann, Aaron M. Goldfain, and Vinothan N. Manoharan**

**Movie S1.** The time-series of images from the assembly experiment using 2 μM protein (Figs. 1, 2, 3, **S1**, **S3**, and **S14**). The time-series is recorded at 1,000 Hz, is shown with a 1,000-frame average, and is sped up by a factor of 33 for playback. The field of view is 9.8 μm on each side. The start of the movie shows a flashing interference pattern that is caused by the sample chamber warping when we inject the protein solution. The flashing ends shortly after the injection is complete. Similar flashing, corresponding to injection of solution, can be seen in each of the following movies.

**Movie S2.** The time-series of images from the assembly experiment using 1 μM protein (Fig. **S6**). The time-series is recorded at 100 Hz, is shown with a 300-frame average, and is sped up by a factor of 66 for playback. The field of view is 14 μm on each side. The illumination beam is blocked for a short time approximately halfway through the movie, just before 2 μM protein is added. In the first half of the movie, where 1 μM protein is in the imaging chamber, a few particles are seen adsorbing to the coverslip, but no particles are seen growing on the coverslip. In the second half of the movie, where 2 μM of protein is in the imaging chamber, a number of particles are seen growing on the coverslip.

**Movie S3.** The time-series of images from the assembly experiment using 1.5 μM protein (Figs. 3 and **S9**). The time-series is recorded at 1,000 Hz, is shown with a 1,000-frame average, and is sped up by a factor of 33 for playback. The field of view is 9.8 μm on each side.

**Movie S4.** The time-series of images from the assembly experiment using 4 μM protein (Figs. 3 and **S10**). The time-series is recorded at 1,000 Hz, is shown with a 1,000-frame average, and is sped up by a factor of 33 for playback. The field of view is 9.8 μm on each side.

**Movie S5.** The time-series of images from the control experiment using 2 μM protein with no RNA on the coverslip (Fig. **S3**). The time-series is recorded at 1,000 Hz, is shown with a 1,000-frame average, and is sped up by a factor of 33 for playback. The field of view is 9.8 μm on each side.

### References

1. Strauss JH, Sinsheimer RL (1963) Purification and properties of bacteriophage MS2 and of its ribonucleic acid. *J Mol Biol* 7(1):43–54.
2. Sugiyama T, Hebert RR, Hartman KA (1967) Ribonucleoprotein complexes formed between bacteriophage MS2 RNA and MS2 protein *in vitro*. *J Mol Biol* 25(3):455–463.
3. Borodavka A, Tuma R, Stockley PG (2012) Evidence that viral RNAs have evolved for efficient, two-stage packaging. *Proc Natl Acad Sci* 109(39):15769–15774.
4. Ortega-Arroyo J, Cole D, Kukura P (2016) Interferometric scattering microscopy and its combination with single-molecule fluorescence imaging. *Nat Protoc* 11(4):617–633.
5. Dulin D, Barland S, Hachair X, Pedaci F (2014) Efficient illumination for microsecond tracking microscopy. *PLOS ONE* 9(9):1–9.
6. Moerner W, Fromm DP (2003) Methods of single-molecule fluorescence spectroscopy and microscopy. *Rev Sci Instrum* 74(8):3597–3619.
7. Allan D, Caswell T, Keim N, van der Wel C (2016) Trackpy v0.3.2; doi: 10.5281/zenodo.60550.
8. Goldfain AM, Garmann RF, Jin Y, Lahini Y, Manoharan VN (2016) Dynamic measurements of the position, orientation, and DNA content of individual unlabeled bacteriophages. *J Phys Chem B* 120(26):6130–6138.
9. Joo C, Ha T (2012) Single-molecule FRET with total internal reflection microscopy. *Cold Spring Harb Protoc* 2012(12):1223–1237.
10. Carey J, Uhlenbeck OC (1983) Kinetic and thermodynamic characterization of the R17 coat protein-ribonucleic acid interaction. *Biochemistry* 22(11):2610–2615.
11. Foreman-Mackey D, Hogg DW, Lang D, Goodman J (2013) emcee: The MCMC hammer. *Publications of the Astronomical Society of the Pacific* 125(925):306.
12. Zhang DY, Winfree E (2009) Control of DNA strand displacement kinetics using toehold exchange. *J Am Chem Soc* 131(47):17303–17314.
13. Happel J, Brenner H (2012) *Low Reynolds number hydrodynamics: with special applications to particulate media*. (Springer Science & Business Media) Vol. 1.
14. Berg HC (1993) *Random walks in biology*. (Princeton University Press), p. 39.